Electronic structure of Pd: Compton scattering, soft-x-ray emission and x-ray photoelectron spectra

R. Podloucky*

Institut fur Technische Elektrochemie, Technical University of Vienna, Getreidemarkt 9, A-1060 Vienna, Austria

R. Lässer

Institut fur Festkorperforschung, KFA Julich, D-5170 Julich, Germany

E. Wimmer and P. Weinberger

Institut fur Technische Elektrochemie, Technical University of Vienna, Getreidemarkt 9, A-1060 Vienna, Austria

(Received 14 December 1978)

The electronic structure of Pd has been calculated in a self-consistent manner using the nonrelativistic augmented-plane-wave (APW) method and the Hedin-Lundqvist local-exchange–correlation approximation. Relativistic effects are discussed in terms of the relativistic Korringa-Kohn-Rostoker method for the self-consistent crystal potential. On the basis of the APW results theoretical intensities for the $L\beta_2$ emission spectrum and the Al-$K\alpha$ valence photoelectron spectrum have been calculated and are compared with results of previous experiments. Compton profiles for single-crystalline Pd have been measured and these are compared to the theoretical profiles, obtained from the APW crystal wave functions. In all cases the agreement with experiment is satisfactory.

I. INTRODUCTION

In this paper the results of experimental and theoretical investigations of the electronic structure of Pd are reported. Experimentally, measurements of Compton profiles for single-crystal specimen have been carried out; theoretically, a self-consistent nonrelativistic augmented-plane-wave (APW) band structure, calculated by means of the Hedin-Lundqvist[1,2] local-exchange–correlation approach, is presented. Furthermore, a relativistic Korringa-Kohn-Rostoker (KKR) calculation using the self-consistent APW-potential has been done for the directions [100], [110], and [111]. On the basis of the APW ground-state band structure, the $L\beta_2$ emission spectrum, the Al-$K\alpha$ photoelectron spectrum and Compton profiles have been calculated and are compared with experimental data. Since the corresponding experimental techniques represent different methods to map out the electronic structure of matter, they permit a critical assessment of the calculated electronic structure to be made.

A number of theoretical investigations of the electronic structure of Pd using the relativistic or nonrelativistic approach, have been reported in the literature.[3-7] All of these have in common that they were not performed self-consistently and that an $X\alpha (\alpha = 1)$ local-exchange–correlation potential was applied. Recently, a nonrelativistic, self-consistent band structure based on KKR method and Hedin-Lundqvist exchange-correlation has also been published.[8] In spite of many experimental results on Pd, no data of the Compton scattering in single crystals have been reported until now.

II. COMPUTATIONAL METHODS

A. Band structure

The energy band structure of Pd (lattice constant $= 7.3530$ a.u.) has been calculated quasi-self-consistently by means of the nonrelativistic APW method,[9,10] exchange and correlation being treated in terms of the Hedin-Lundqvist approach.[1,2] Within the muffin-tin sphere of radius $R = 2.5997$ a.u. the partial-wave expansion is truncated at a maximum angular momentum quantum number of 12. The plane-wave expansion is restricted to $|\vec{k}+\vec{g}| \leq (\pi/a)\sqrt{80}$, $\vec{k}$ being a vector in the Brillouin zone and $\vec{g}$ a reciprocal-lattice vector. A maximum of 40 basis functions, corresponding to equivalent irreducible representations of the little group of the wave vector $\vec{k}$, are taken into account. The resulting self-consistent muffin-tin charge density is based on a grid of 512 $\vec{k}$ points in the Brillouin zone and refers to a maximum deviation of 1mRy for one-electron energies in two subsequent iterations.

In order to discuss the relativistic effects rigorously, the relativistic KKR method[11-13] and its nonrelativistic limit have been applied to the self-consistent crystal potential. The KKR results correspond to a muffin-tin sphere radius of 2.5857 a.u. and a cutoff of the angular momentum quantum number at $l = 2$.

B. X-ray emission and x-ray photoelectron spectra

The theoretical intensity for the Pd-L emission spectrum has been calculated in terms of an l-like local density of states and radial transition probabilities.[14-16] For the theoretical x-ray photoelectron spectrum two cases are considered: (i) constant transition moments and (ii) transition moments using a plane-wave approximation for the photoelectron wave function.[17] For both types of spectra, broadening is simulated parametrically.

C. Compton scattering

Considering only the nonrelativistic limit, the Compton cross section is given within the first Born approximation by[18]

$$\frac{d\sigma}{d\Omega d\omega} = \left(\frac{d\sigma}{d\Omega}\right)_{\text{Th}} \frac{\omega_2}{\omega_1} S(\vec{k}_c, \omega) \qquad (1)$$

with $\omega = \omega_1 - \omega_2$, $\vec{k}_c = \vec{k}_1 - \vec{k}_2$, and $(d\sigma/d\Omega)_{\text{Th}} = \frac{1}{2}r_0^2(1 + \cos^2\theta)$, where ω_1 and ω_2 are the energies and $\vec{k}_1$ and $\vec{k}_2$ the wave vectors of the incident and the scattered photon, respectively. For averaged photon polarizations, the Thomson cross section $(d\sigma/d\Omega)_{\text{Th}}$ is given in terms of the electron radius $r_0 = e^2/mc^2$ and the scattering angle θ. The dynamical structure factor $S(\vec{k}_c, \omega)$ is calculated within the so-called impulse approximation (IA).[19,20] Applying the IA requires that the photon interact only with one electron and that the recoiled electron is scattered instantaneously into a free-plane-wave state. Then $S(\vec{k}_c, \omega)$ is given by

$$S(\vec{k}_c, \omega) = (2\pi\hbar)^{-3} \int n(\vec{p}) \delta\left(\omega - \frac{\hbar^2 k_c^2}{2m} - \frac{\hbar(\vec{k}_c \cdot \vec{p})}{m}\right) d\vec{p},$$

$$(2)$$

where $\vec{p}$ is the momentum of the electron before being scattered and $n(\vec{p})$ the momentum density for the ground state of the electronic system. In terms of the single-particle approximation, the electron momentum density $n(\vec{p})$ at $T = 0\,°K$ is defined by a sum of occupied Bloch states for a given wave vector $\vec{k}$

$$n(\vec{p}) = \sum_j \left| \int \Psi_{\vec{k}}(\vec{r}, E_{\vec{k}}^j) \exp(-i\vec{p} \cdot \vec{r}/\hbar) d\vec{r} \right|^2, \qquad (3)$$

where $\Psi_{\vec{k}}(\vec{r}, E_{\vec{k}}^j)$ denotes the one-electron wave function of an occupied state with energy $E_{\vec{k}}^j$. Applying the laws of conservation of energy and momentum and using a laboratory-coordinate system with the z axis lying in direction of $\vec{k}_c$, Equation (1) can be rearranged to

$$\frac{d\sigma}{d\Omega d\omega} = C(\omega_1, \omega_2, \theta) J(q), \qquad (4)$$

where the Compton profile $J(q)$ is defined as

$$J(q) = (2\pi\hbar)^{-3} \int n(\vec{p}) \delta(p_z - q) d\vec{p} \qquad (5)$$

with

$$q = (\omega - \hbar^2 k_c^2/2m)/k_c$$

and

$$p_z = (\hbar/m)\vec{p} \cdot \vec{k}_c/k_c .$$

Equation (4) is also valid for relativistic scattering of high-energy photons, but q and the factor $C(\omega_1, \omega_2, \theta)$, which relates the differential cross section to the Compton profile $J(q)$, are much more complicated than in the nonrelativistic case.[21]

The theoretically calculated Compton profiles are based on the self-consistent APW band-structure results. For the APW Compton scattering matrix elements[22] only states of the conduction band have been treated as Bloch states, the contributions from the core ($1s^2 2s^2 2p^6 3s^2 3p^6 3d^{10}$) and the semi-core ($4s^2 4p^6$) have been added from the tables of Biggs et al.[23] The grid in momentum space is determined by the grid of $\vec{k}$ vectors used in the APW calculation. Since the expansion in reciprocal-lattice vectors has covered about 100 zones, approximately 57 000 different vectors in momentum space have been generated. The l cutoff is the same as in the APW method, namely, 12.

III. RESULTS

A. Band structure

Figure 1 shows the nonrelativistic self-consistent APW energy bands along the [100], [111], and [110] $\vec{k}$ ray and along directions in the hexagonal $(L - W)$ and quadratic $(W - X)$ faces of the Brillouin zone. In Fig. 2 the density of states (DOS) histogram $g(E)$ is shown together with the d-like local DOS, corresponding to the applied grid of 512 $\vec{k}$ points in the Brillouin zone and an energy interval of 25 mRy. In Fig. 2, dashed areas denote the remainder of $x_l(E)$, i.e., the sum of the l-like local DOS with $l \neq 2$ and the energy distribution function of the charges in the region of constant potential. In Table I, the l-like total charges within the muffin-tin sphere and the total charges in the region of constant potential are listed for the semi-core and valence-energy region. The calculated Fermi energy is 0.543 Ry.

In Fig. 3 the differential κ-like contributions to the single-site differential Friedel sum[24] for $l = 2$, corresponding to the self-consistent crystal potential, are displayed. These single-site quantities not only provide a reasonable qualitative description for the d resonance, but also show the signifi-
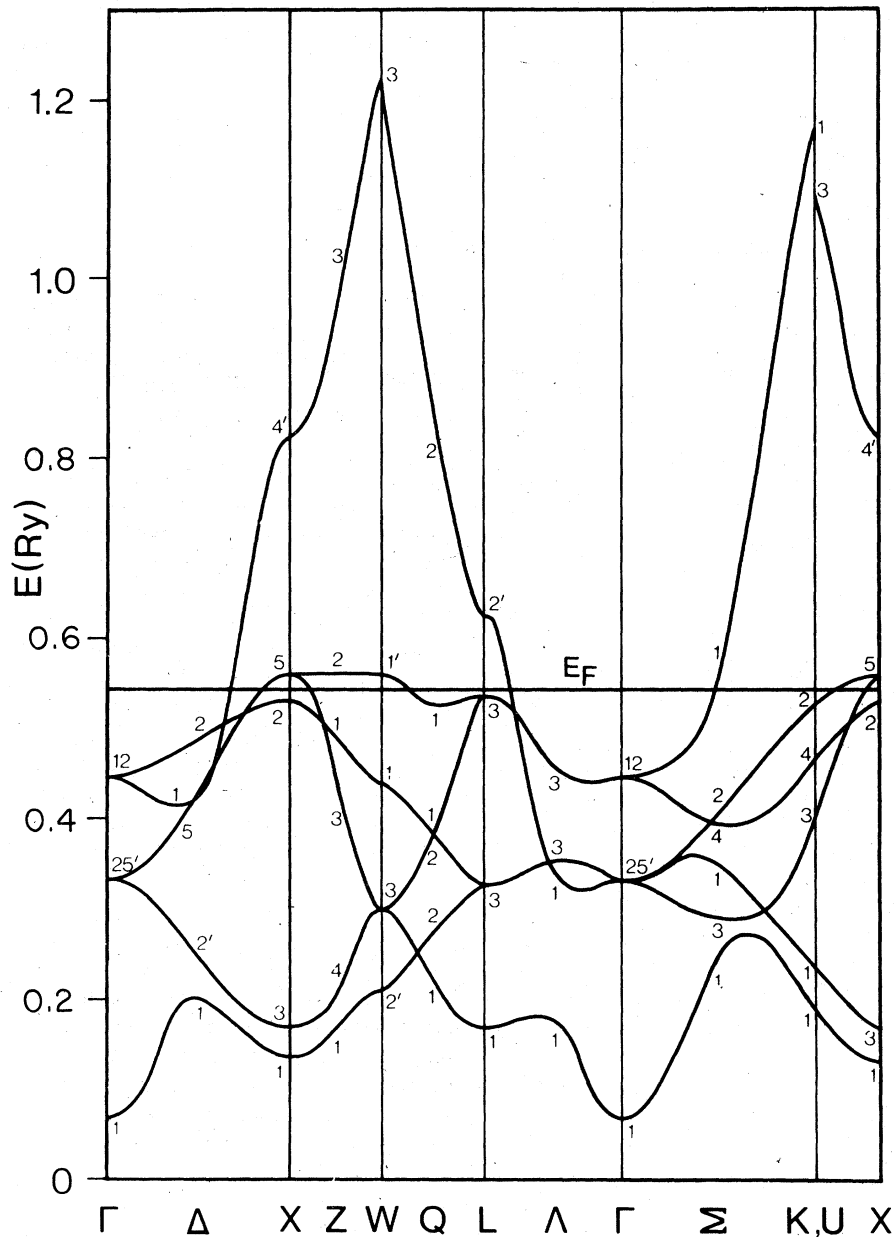
FIG. 1. Nonrelativstic self-consistent APW band structure for Pd along high-symmetry axes.

cance of a rigorous treatment of relativistic effects. In a Pauli-Schrödinger type approach, the difference of the $d^{3/2}$-and $d^{5/2}$-resonance energies corresponds to the so-called spin-orbit splitting. Figure 4 shows a comparison of the relativistic energy bands with their nonrelativistic counterparts as calculated with the KKR method using the self-consistent crystal potential of our APW calculation. The energy bands are shown for the [100], [111], and [110] $\vec{k}$ rays. In each case the left-hand part of the figure refers to the relativistic calculation. In the case of the relativistic
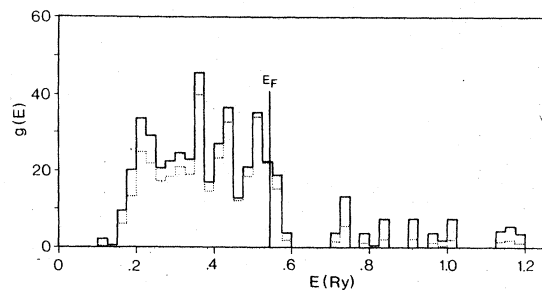
FIG. 2. Density of states (histogram) $g(E)$ and d-like local density of states $\chi_d(E)$. Dashed areas correspond to the difference of $g(E) - \chi_d(E)$.

TABLE I. l-like total charges within the muffin-tin sphere and charge in the region of constant potential as compared to the free atom. The table refers to the self-consistent APW results.

	Semi-core		Valence					Total	
	s	p	s	p	d	f	$l>3$	Q_{in}	Q_{out}
Crystal	1.999	5.985	0.386	0.357	8.406	0.058	0.025	45.216	0.784
Free atom	1.999	5.984			8.945			44.927	1.073

approach, it should be noted that the classification of states is according to irreducible projective representations of the point group of the $\vec{k}$ vector ("double group") whereas in the nonrelativistic limit the irreducible vector representations of the point group of $\vec{k}$ ("single group") are applied. In Table II the states at the $\vec{k}$ points Γ, X, and L are characterized in terms of κ-like[13] and l-like partial charges. The last column in this table refers to the corresponding nonrelativistic APW eigenvalues.

B. X-ray emission and x-ray photoelectron spectra

A comparison of the experimental $L\beta_2$ emission spectra[25] and the theoretically calculated spectrum is given in Fig. 5(a). In this figure, the experimental spectra 1 and 2 correspond to the un-
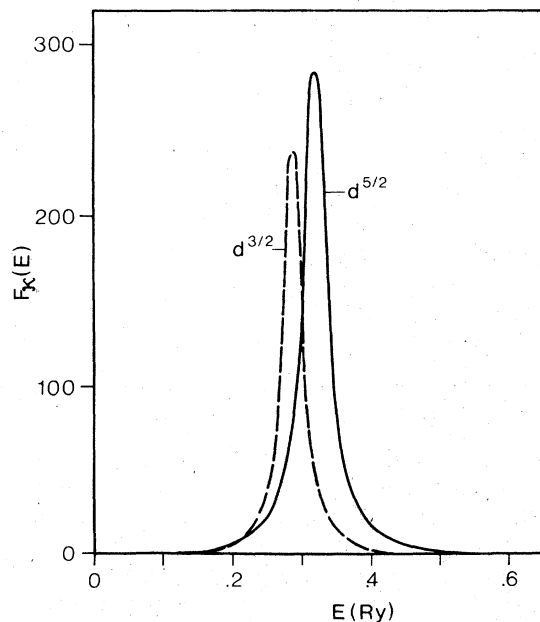
FIG. 3. κ-like single-site differential Friedel summands for $l=2$ corresponds to the self-consistent crystal potential.

corrected and corrected intensities, respectively. The theoretical spectrum is based on the broadening parameters[15,26] $\gamma_0 = 1.0$ eV (lifetime broadening), $W = 0.02$ (energy-dependent valence broadening), and $S = 0.2$ eV (spectrometer resolution) and and on the calculated Fermi energy E_F.

Figure 5(b) shows the experimental Al-$K\alpha$ valence photoelectron spectrum[27] and two theoretical spectra. Spectrum 2 in Fig. 5(b) corresponds to the DOS (Fig. 2). For spectrum 3, transition probabilities are considered in terms of a plane-wave approximation for the photoelectron wave function.[17] Both theoretical spectra correspond to the broadening parameters $\gamma_0 = 0.3$ eV (half-width of the incident photon energies), $W = 0.2$, and $S = 0.5$ eV and are based on the calculated Fermi energy.

C. Compton scattering

Figure 6 shows the electron momentum density (EMD) defined by Eq. (3) for the three principal directions [100], [110], and [111] of the momentum vector $\vec{p}$ with the corresponding parts of the band structure inserted. The bands, which are observable in the EMD according to group theory,[28] are drawn as full lines and the noncontributing bands as dashed lines. In order to analyze the results of the Compton calculation the energy scale (given in Ry) is partitioned into three regions, namely, [0.069, 0.275], [0.275, 0.375], [0.375, E_F]. These regions will be referred to as R1, R2, and R3, respectively. In Fig. 6, the contributions to the EMD are indicated as dash-dotted (R1), dashed (R2), and full lines (R3). The total EMD, which includes all three regions, is drawn as a thick line. As a result of our APW calculation, Table III presents l-like partial charges and charges located outside the muffin-tin sphere for energies belonging to bands, which are observable in the EMD's.

Figure 7 shows the Compton profiles (CP's) as defined in Eq. (5) J_{100}, J_{110}, and J_{111} for the conduction band and orientations of the [100], [110], and [111] axes of the crystal parallel to the laboratory z axis. The contributions from the three

FIG. 4. Relativistic and nonrelativistic energy bands along the [100] (a), [111] (b), and [110] (c) k̄-ray corresponding to the self-consistent crystal potential.

energy regions R1, R2, and R3 and the total profiles are indicated in the same manner as in Fig. 6.

IV. SETUP OF THE COMPTON SCATTERING EXPERIMENT

Our experimental setup is similar to that described previously,[29] but with the following differences: two cylindrical beam channels were used with a mean scattering angle of 172.5° and the γ source consisted of ^{51}Cr (half-life 27.7 days[30]), which emits photons of only one energy (320.076 keV). After n activation the activity of the Cr disc used was 45 Ci. The average energy transfer to an electron in a Compton scattering event is 177 keV, so that the IA (Sec. II) is well satisfied

TABLE II. κ-like and l-like partial charges (%) for states at $\vec{k}=\Gamma$, X and L as calculated by means of the KKR method. The last column refers to the corresponding nonrelativistic APW energy eigenvalues. $\vec{k}$ is in units of $2\pi/a$.

$\vec{k}$	j	$E^j_{\vec{k}}$	Relativistic KKR						j	$E^j_{\vec{k}}$	Nonrelativistic KKR				APW $E^j_{\vec{k}}$
			$s^{1/2}$	$p^{1/2}$	$p^{3/2}$	$d^{3/2}$	$d^{5/2}$	out			s^0	p^1	d^2	out	
000	Γ_6^+	−0.002	68.23					31.77	Γ_1	0.070	66.77			33.23	0.069
	Γ_8^+	0.411				24.68	73.44	1.88	Γ_{12}	0.448			98.09	1.91	0.447
	Γ_7^+	0.316					96.08	3.92	$\Gamma_{25'}$	0.337			95.96	4.04	0.334
	Γ_8^+	0.291				72.35	23.92	3.73							
100	X_6^+	0.107	4.89			34.99	44.21	15.91	X_1	0.136	4.55		78.88	10.57	0.135
	X_7^+	0.485				48.54	48.89	2.58	X_2	0.532			94.16	0.84	0.532
	X_7^+	0.143				39.31	48.06	12.63	X_3	0.171			91.17	8.83	0.170
	X_6^+	0.509	0.03			57.20	42.11	0.65	X_5	0.562			99.49	0.51	0.562
	X_7^+	0.531				5.80	93.20	1.00							
$\frac{111}{222}$	L_6^+	0.132	15.02			32.70	39.65	12.63	L_1	0.171	13.86		73.35	12.79	0.169
	$L_{4,5}^+$	0.280				77.43	17.10	6.47	L_3	0.329			94.77	5.23	0.326
	L_6^+	0.307	0.02			4.78	89.61	5.69							
	$L_{4,5}^+$	0.501				18.32	80.65	1.03	L_3	0.537			98.92	1.08	0.537
	L_6^+	0.487	0.11			51.61	46.90	1.39							

even for the strongly bound electrons of the K shell in Pd. The resolution full width at half-maximum (FWHM) of the detector system (Princeton-Gamma-Tech, IGP 210, RG-11C) was measured by means of the isotopes [241]Am, [57]W, [182]Ta, [133]Ba and is shown in Fig. 8. At the position of the Compton peak (142.42 keV) the FWHM of the resolution is 538 eV. When the beam divergence is taken into account, the overall energy resolution at the Compton peak deteriorates to 561 eV or 0.374 a.u.

The Pd samples used were single-crystalline slices 1.74 mm thick with normals parallel to the three main symmetry directions. In order to correct for multiple scattering one [100] single crystal of thickness 0.40 mm was measured. The samples had a mosaic structure of 0.5°. They were mounted on a goniometer in a vacuum chamber in such a way that the scattering vector was parallel to one of the main symmetry directions within an error of ±1°. For the determination of the anisotropy more than 150000 counts/channel (one channel corresponds to 83.2 eV or 0.055 a.u.) were collected in the Compton peak for every direction within 2.7 days. In the case of the thin sample about 40000 counts/channel at the maximum of the Compton profile were collected within 3.7 days.

The Compton profiles obtained from the experiments were processed by subtracting the background contribution after fitting the background

data to the Pd data in the region above the 320 keV line, applying corrections for the energy-dependent detector efficiency and for the scattering cross section and taking into account the absorption of the photons in the sample. The energy was then transformed into momentum scale and the area under the profile normalized according to the number of electrons per atom. For Pd-[100], the measured profiles were corrected for multiple scattering by extrapolating[31] the profiles, measured at different thicknesses, to thickness zero. The result is shown in Fig. 9. The statistical error is smaller than the size of the circles.

Figure 10 shows a typical, unsmoothed anisotropy curve as obtained by subtracting the Compton profiles for the orientations [110] and [100] channel by channel. The data for positive and negative q values were averaged and smoothed by a nine-point least-squares procedure. To correct for the multiple scattering in the anisotropic data, the ratio of the Compton profile peak $J(0)$ of sample thickness 0.40 mm to the one of thickness 1.74 mm was calculated and the anisotropic data were multiplied with the factor 1.06 thus obtained.

V. DISCUSSION

A. Band structure

The band structure of Pd (Fig. 1) is characterized by a system of d-like bands, which is cut
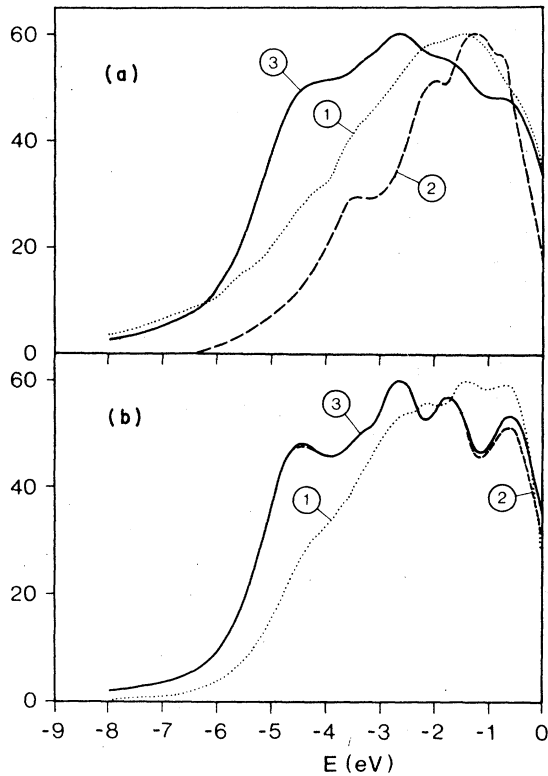
FIG. 5. (a) Comparison of experimental spectra (1) and (2) (Ref. 25) with the calculated $L\beta_2$ emission spectrum (3). (b) Comparison of the experimental Al-$K\alpha$ photoelectron spectrum (1) (Ref. 27) with theoretically calculated intensities. Spectrum (2) corresponds to the broadened density of states. For spectrum (3) electric dipole transition probabilities are used within the plane-wave approximation for the photoelectron wave function.

through by a very broad s-like band. The Fermi energy is situated almost at the edge of the d-band system just below X_5. Since the s-like band is nearly free-electron-like, the contribution of the s-like DOS is rather small. This can be seen in Fig. 2, where the d-like local DOS dominates the structure of the total DOS. Since the bands have different characters, relativistic effects will not cause a uniform shift of eigenvalues. The $d^{3/2}$- and $d^{5/2}$-like contributions to the single-site differential Friedel sum in Fig. 3 show that the difference of the resonance energies is about 0.03 Ry.

In Fig. 4, the relativistic effects on the band structure can be seen in detail. The s-like states are shifted substantially towards lower energies ($\Gamma_1 - \Gamma_6^+ = 0.073$ Ry), whereas for d-like states this shift is much less pronounced ($X_3 - X_7^+ = 0.029$ Ry). The splitting of multidimensional irreducible vector representations is nearly constant [$\Gamma_{25'}$: (Γ_7^+

$- \Gamma_8^+$) $= 0.025$ Ry, X_5:($X_7^+ - X_6^+$) $= 0.022$ Ry] and is approximately equal to the value predicted by the single-site estimate (Fig. 3). In the relativistic case some of the intersections of the nonrelativistic energy bands are removed. Table II shows that for all cases where no intersection occurs in the nonrelativistic limit, the relativistic wave functions are slightly more contracted than their nonrelativistic counterparts. However, whenever such intersections occur, relativistic states are more delocalized than the nonrelativistic ones. Figure 4 and Table II show that relativistic effects have to be discussed rather carefully and only on the basis of totally compatible calculations, i.e., by actually calculating the nonrelativistic limit for the same potential. It should be noted that the relativistic effects which were obtained in the present calculations agree very well with other results.[3,4,7]

B. X-ray emission and x-ray photoelectron spectra

Because the total DOS is dominated strongly by the d-like local DOS (Fig. 2), the theoretical spectra in Fig. 5 are shaped mainly by the d-like local DOS. Furthermore, for the L-emission spectrum only the s- and d-like local DOS can contribute to the intensity.[13-15] The dominance of the d-like local DOS is also illustrated in the x-ray photoelectron spectra (XPS) results, where there is almost no difference between the two theoretical spectra. In terms of the plane-wave approximation for the photoelectron wave functions (spectrum 3), the contribution due to electric dipole transition probabilities seems to be insignificant. The theoretical XPS results agree well with the experimental spectrum as far as the location of peaks and bumps is concerned. However, the intensity for the shoulder at -4.5 eV is overestimated in both theoretical spectra. It should be noted, that Smith et al.[27] obtained very similar results when comparing the DOS for Rh, Pd, Ir, Pt, and Au with the corresponding XPS data. In comparison to the XPS, the x-ray emission spectrum (XES) is less structured. Again the bump at -4.5 eV is exaggerated in the theoretical intensity. Since the L_2 and L_3 emissions are well separated in energy, the nonrelativistic approach, which was applied to the radial transition moments,[14,15] is justified[16] and cannot be the reason for the above-mentioned exaggeration.

C. Compton scattering

The expansion of the electron wave function $\Psi_{\vec{k}}(\vec{r}, E_{\vec{k}}^j)$ and the operator $\exp(-i\vec{p}\cdot\vec{r}/\hbar)$ of Eq. (3)
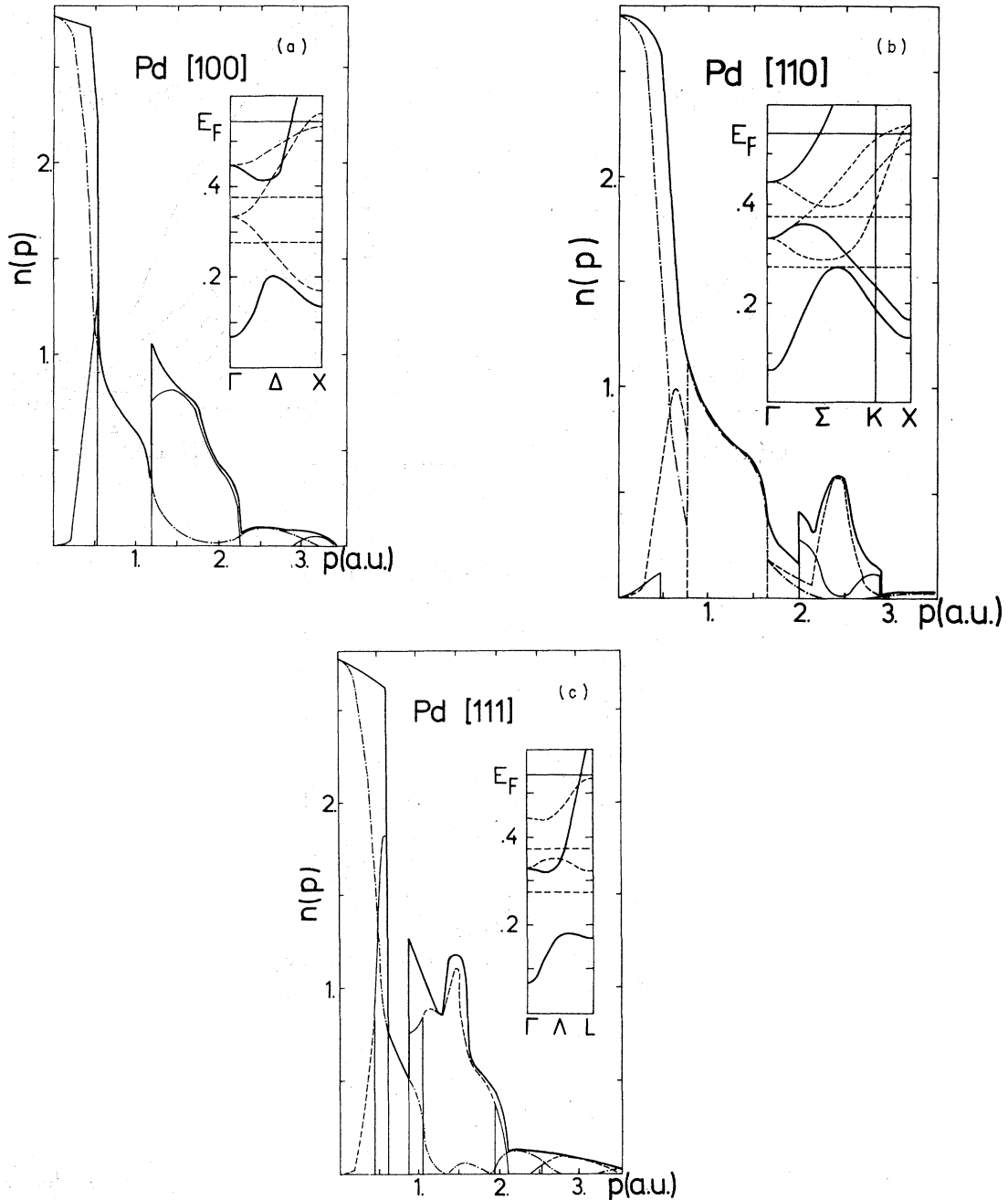
FIG. 6. Electron momentum density of the conduction band in arbitrary units and, as inserts, the corresponding part of the band structure with observable (full lines) and not observable (dashed lines) bands. The total momentum density (thick full line) is split up in contributions from the energy regions R1 (dash-dotted line), R2 (dashed line), and R3 (full line).

into spherical harmonics yields an estimate for the spherically averaged EMD for small p

$$n(p, E_{\mathbf{k}}^j) \approx c_0(E_{\mathbf{k}}^j) + \sum_{l>0} c_l(E_{\mathbf{k}}^j) p^{2l}, \tag{7}$$

where c_l is the l-like partial charge. This estimate is valid provided that most of the electrons are located inside the muffin-tin spheres as is the case for Pd (Table I). Applying Eq. (7), only the R1 term containing representation Γ_1 gives a non-
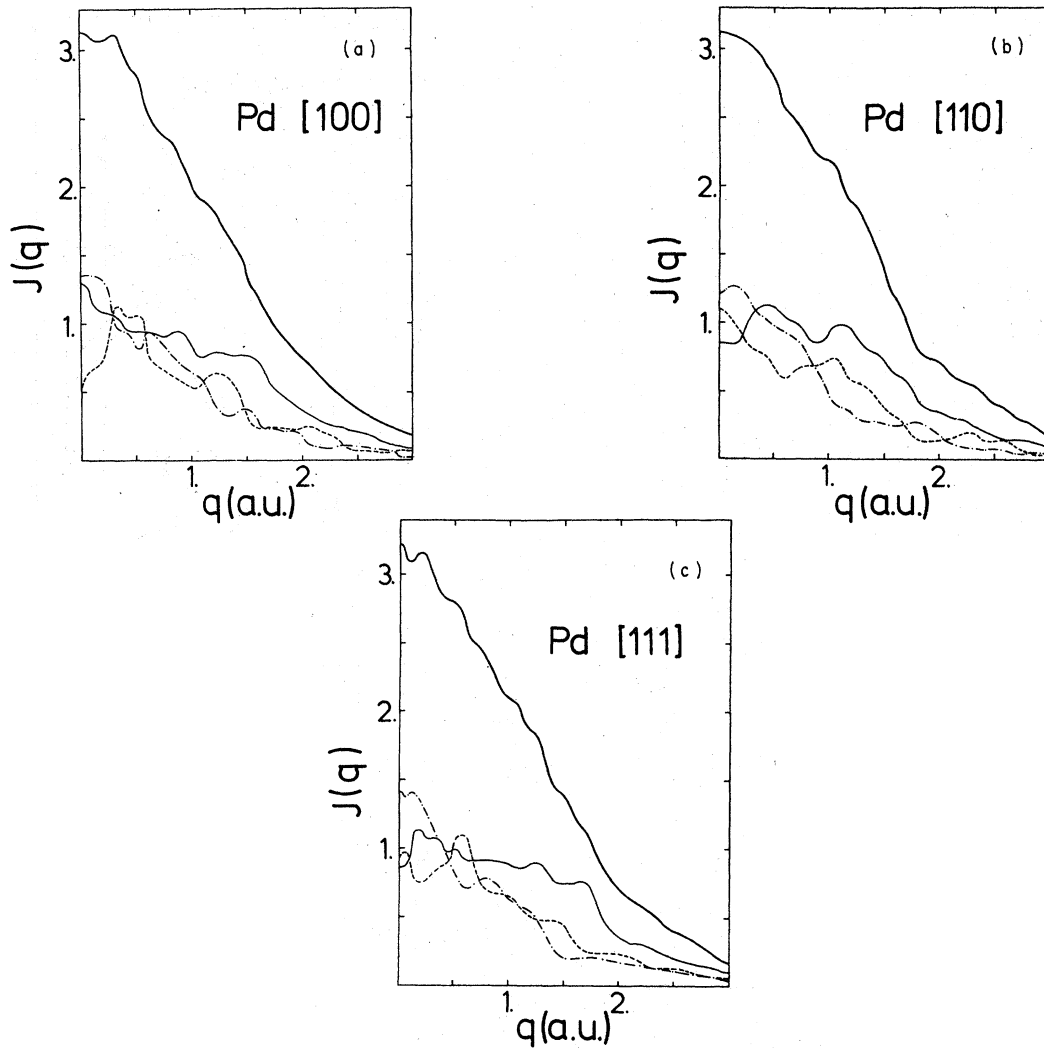
FIG. 7. Total Compton profiles (thick full line) for the conduction band with the contributions from the energy regions R1 (dash-dotted line), R2 (dashed line), and R3 (full line).
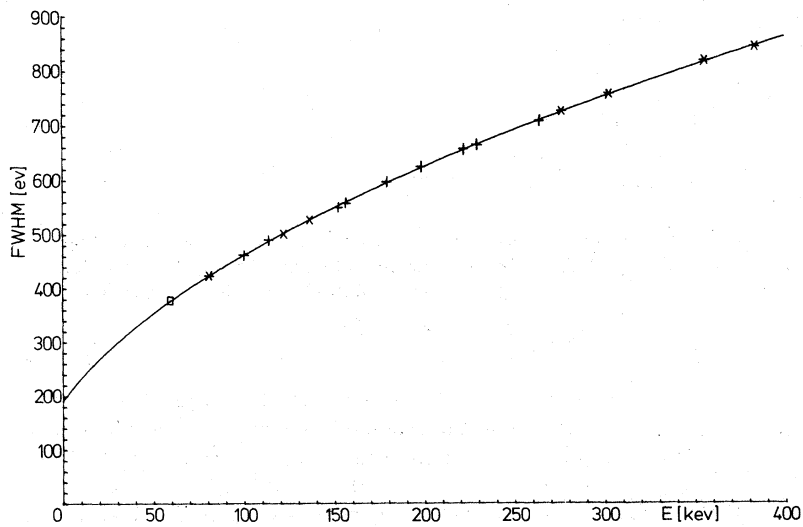
FIG. 8. Detector resolution (FWHM) vs energy of the photons measured by means of the radioactive isotopes ^{241}Am(□), ^{57}Co(✗), ^{182}Ta(+), and ^{133}Ba(*).
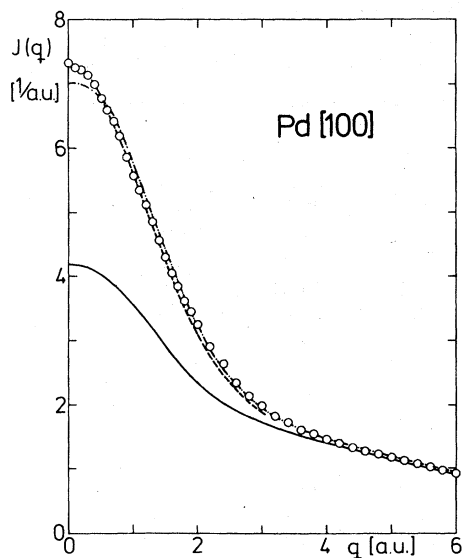
FIG. 9. Comparison of the total Compton profile J_{100} with experimental (open circles) and calculated values (APW = dashed line, core contribution = solid line, free atom (Ref. 23) = dash-dotted line). The theoretical APW profile has been folded with the experimental resolution.

vanishing contribution for $p = 0$. Furthermore, for very small p the R1 term is the dominant one as can be seen from Fig. 6.

The total EMD's for the directions [100] and [111] show major discontinuities near $p = 0.5$, 1.2 a.u. and $p = 0.6$, 0.85 a.u., respectively [Figs. 6(a) and 6(c)]. These discontinuities are produced by the R3 contributions, whereas the R3 component of the [110] EMD produces only small jumps near $p = 0.5$ and 2.0 a.u. [Fig. 6(b)]. The discontinuities are caused by the crossing of the highest observable bands with the Fermi energy (inserts in Fig. 6). The crossing restricts the set of $\vec{k}$ vectors labeling occupied states. The set of $\vec{p}$ vectors, which give a nonvanishing contribution to the EMD's, is also restricted, because the $\vec{p}$ vectors can differ from the $\vec{k}$ vectors only by vectors of the reciprocal lattice.[28] In the same manner the R1 and R2 jumps can be explained by the crossing of observable bands with the energies 0.275 and 0.375 Ry. From Table III it can be estimated that the hybridization of the highest observable band at the Fermi energy is much larger along the directions $\Gamma\Delta X$ and $\Gamma\Lambda L$ (e.g., for $\Gamma\Delta X$ about 20% s-, 25% p-, and 30% d-like charges) than for $\Gamma\Sigma K/X$ (5% s, 5% p and 80% d). According to Eq. (7), the contribution of R3 to the [100] and [111] EMD at small p's increases much faster with increasing p than the contribution for the [110] EMD. For
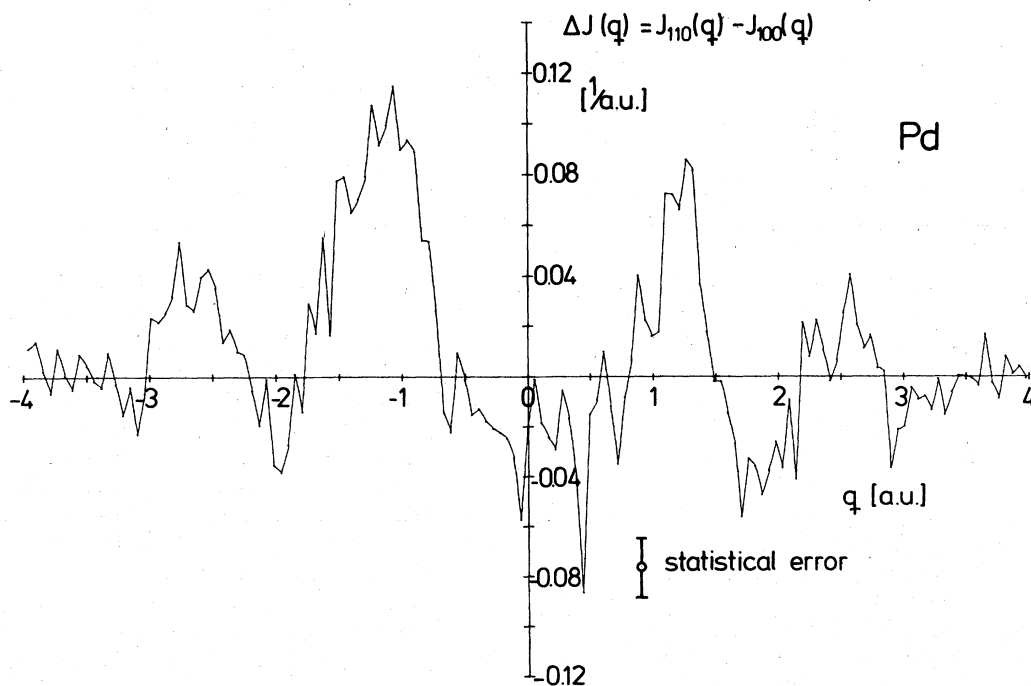
FIG. 10. Experimental channel to channel difference of $(J_{110} - J_{100})$.

TABLE III. l-like partial charges (%) of the APW calculation with $\vec{k}$ along the three cubic main directions. Values are only listed for bands, which are observable in the corresponding electron momentum density. (a) and (b) may be completed using (c) by adding Γ_1', Γ_{12} and Γ_1', Γ_{25}', respectively. $\vec{k}$ is in units of $2\pi/a$.

(a)	$\vec{k}$	j	$E_{\vec{k}}^j$	s	p	d	out
	$\frac{1}{4}00$	Δ_1	0.120	62.22	4.93	1.20	31.65
			0.418	0.84	0.19	95.33	2.74
	$\frac{1}{2}00$	Δ_1	0.201	29.80	8.47	37.49	23.99
			0.425	19.36	10.52	55.28	13.60
	$\frac{3}{4}00$	Δ_1	0.163	7.48	1.70	74.07	16.45
			0.638	20.27	39.35	13.47	25.06
	100	X_1	0.135	4.66		79.31	15.97
		X_4'	0.842		66.85		29.39
(b)							
	$\frac{1}{8}\frac{1}{8}\frac{1}{8}$	Λ_1	0.108	63.81	3.55	1.09	31.54
			0.323	0.43	0.98	93.20	4.46
	$\frac{1}{4}\frac{1}{4}\frac{1}{4}$	Λ_1	0.178	40.11	5.29	31.13	23.28
			0.343	12.61	12.23	58.73	15.48
	$\frac{3}{8}\frac{3}{8}\frac{3}{8}$	Λ_1	0.178	17.74	0.79	67.81	13.40
			0.498	15.96	37.71	14.93	30.36
	$\frac{1}{2}\frac{1}{2}\frac{1}{2}$	L_1	0.169	14.17		73.70	12.00
		L_2'	0.626		59.86		38.35
(c)							
	000	Γ_1	0.069	68.21			31.79
		Γ_{25}'	0.334			96.10	3.19
		Γ_{12}	0.447			98.19	1.32
	$\frac{1}{4}\frac{1}{4}0$	Σ_1	0.164	55.67	8.30	5.53	30.44
			0.360	0.62	1.52	92.55	4.41
			0.476	1.70	0.92	94.46	2.16
			0.273	11.00	3.24	74.84	10.10
	$\frac{1}{2}\frac{1}{2}0$	Σ_1	0.314	6.49	12.57	63.30	16.96
			0.731	16.38	15.78	53.53	14.04
			0.189	2.57	0.50	83.84	12.46
	$\frac{3}{4}\frac{3}{4}0$	K_1	0.237	0.08	6.75	81.87	11.02
			1.167	14.08	34.27	19.33	25.14
	100	X_1	0.135	4.66		79.31	15.97
		X_3	0.170			91.61	8.28

this reason, the discontinuities caused by crossing the Fermi energy are much more pronounced for the [100] and [111] EMD than they are for the [110] EMD.[32]

The CP for the three principal directions J_{100}, J_{110}, and J_{111} show remarkable structures (Fig. 7), which are produced by the complicated Fermi surface[3,4] and by the strongly localized d electrons (Table I). In other words, the shape of the CP's is the result of the discontinuities and high momentum contributions of the EMD's (Fig. 6). The calculated valence-band CP's for $q=0$ [$J_{100}(0) = 3.129$, $J_{110}(0) = 3.091$, and $J_{111}(0) = 3.244$ 1/a.u.] are larger than the corresponding CP of the free atom[23] [$J(0) = 2.822$ 1/a.u.]. This in fact reflects the partial occupation of s and p states, which are unoccupied in the atomic case, when the solid-state

bonding is built up (Table I). There are noticeable peaks in J_{100} at $q = 0.35$ a.u. (mainly from R2) and in J_{111} at $q = 0.2$ a.u. (mainly from R1 and R3). For $q > 0.7$ a.u., the contribution of R3 determines the structure of the CP's (Fig. 7).

In Fig. 9 the experimental total J_{100} is compared with the calculated one, which is convoluted with the experimental resolution function. There is excellent agreement expecially for small q values. In the region $2 < q < 3$, the theoretical J_{100} is slightly smaller than the experimental CP. This can be explained by the truncation of the reciprocal-lattice expansion (Sec. II). Because of this truncation, the integration of the total valence CP gives only 9.13 electrons instead of 10. The neglect of high Fourier components affects only the isotropic part of the EMD's and CP's. The differences

of the Compton profiles (DCP's) for different directions are in excellent agreement with the experiment when $q > 2$ (Fig. 11).

All of the experimental and calculated DCP's for the main directions are in good agreement for $q > 0.7$ and also for the DCP $(J_{110} - J_{100})$ when $q < 0.7$. Deviations occur at small momenta for the two DCP's $(J_{100} - J_{111})$ and $(J_{110} - J_{111})$. The comparison of our experimental data with that for Cu and Ni (Ref. 33) confirms that the signs of our experimental results at $q = 0$ are reasonable (Fig. 11). Therefore, it must be assumed that the theoretical J_{111} is too big in the neighborhood of $q = 0$. The discrepancies at small momenta are attributed to the simplifications chosen for the solid-state

model of our calculation (Sec. II). There are three possibilities: relativistic effects, non-muffin-tin effects, and effects derived from the local-exchange–correlation potential used.

The relativistic energy shifts are less than 0.073 Ry (~ 1 eV). Concerning just the d band, the shifts and splittings according to different j values are about 0.03 Ry (~ 0.5 eV), whereas the FWHM of the experimental resolution of 0.374 a.u. corresponds to 0.16 Ry (~ 2 eV) in the band structure. Table II shows that the relativistic partial d charges are only slightly changed ($< 4\%$, Table II). In addition, for the DCP's at high momenta ($q > 2$) in Fig. 11 there is no broadening of the experimental curves compared with the calculated ones. Such a broad-
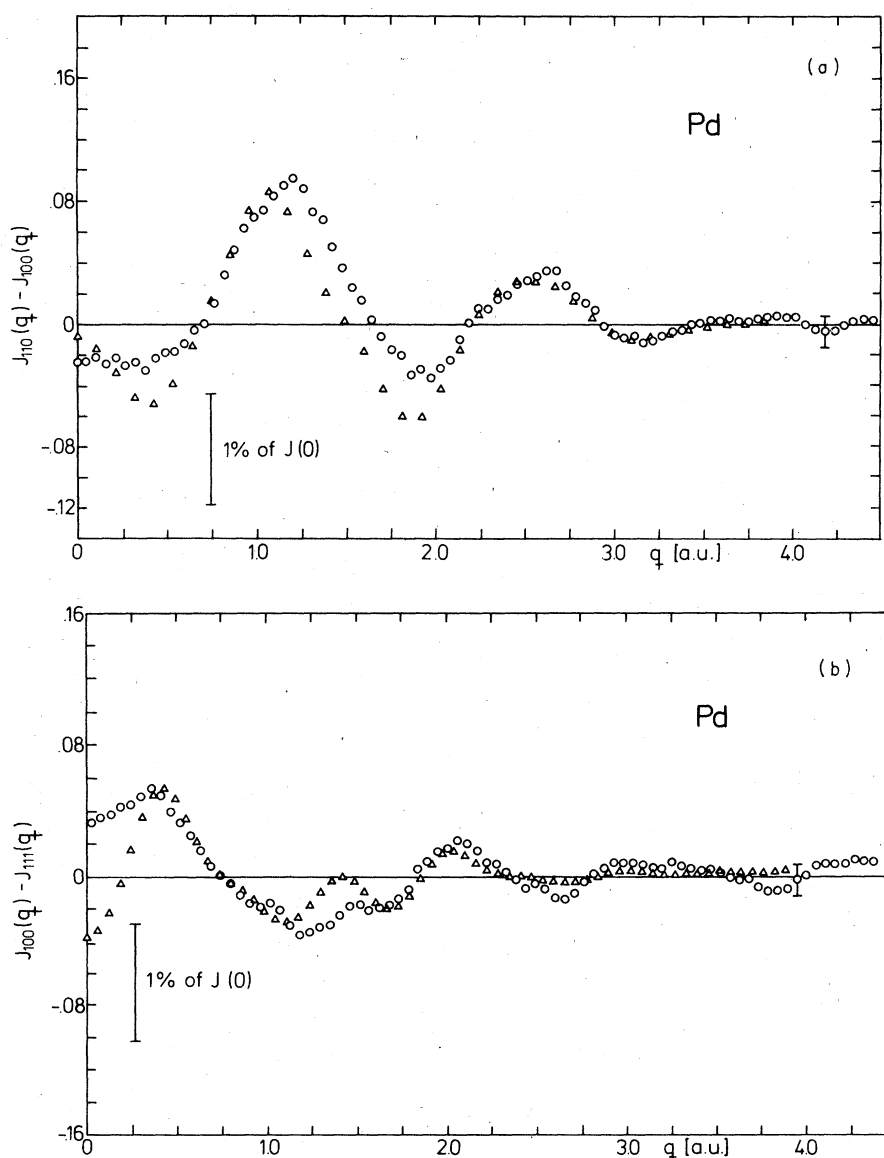
FIG. 11. Differences between the Compton profiles as obtained from the experimental (open circles) and folded theoretical (open triangles) values.
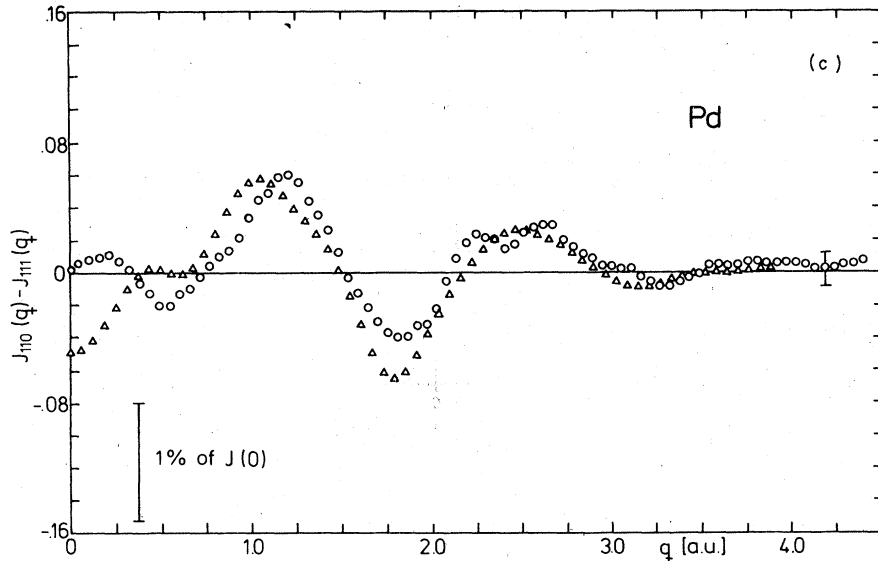
FIG. 11. (*Continued*)

ening would indicate a relativistic contraction of the d wave functions. In this way, the relativistic corrections seem to be small for the CP's.

Non-muffin-tin effects only cause little changes in the band structure of Pd (Ref. 6). The energy shifts are less than 0.012 Ry (~ 0.2 eV). The major effect are the corrections from outside the muffin-tin spheres, where there are less than 8% of the valence electrons (Table I). Thus far, neglecting non-muffin-tin effects seems to be justified.

Simple considerations can be used to find a hint for the source of deviations at $q = 0$. Considering just the EMD's in the three main cubic directions, the contributions to $J_{100}(0)$ consist of four [100]-type EMD's (namely, the projections on the [100] axis of EMD's in the directions [010], [0$\bar{1}$0], [001], and [00$\bar{1}$]) and four [110]-type EMD's. In the same way, $J_{110}(0)$ contains two [100] EMD's, two [110] EMD's, and four [111] EMD's. However, the sensitive $J_{111}(0)$ includes only one type, namely, six [110] EMD's. The [110] EMD is distinguished from the [100] and [111] EMD, since the (110) direction in real space connects the nearest neighbors and favours d-d bonding due to the lobes of the t_{2g} orbitals in this direction. The d bonding properties are reflected by the DCP's at higher momenta ($q > 0.7$). There, the DCP's ($J_{110} - J_{100}$) and ($J_{110} - J_{111}$) show [Figs. 11(a) and 11(c)] distinctly higher anisotropy than ($J_{100} - J_{111}$) [Fig. 11(b)]. This behavior has also been observed for the case of Cu and Ni (Ref. 33). Since the [110] EMD strongly reflects the d-electron features, this EMD (and J_{111} at small momenta) should be sensitive to the limitation that using the local-exchange-correlation approximation, the spatial variation of the

charge density should be sufficiently slow and weak.

VI. CONCLUSION

Using a self-consistent APW method[10] and a local-exchange-correlation approximation of Hedin-Lundqvist type,[1,2] the electronic structure of Pd can be described satisfactorily. The reported band-structure results agree well with experimental data of XES, XPS, and Compton scattering. Since the experimental results are obtained using different methods, they confirm independently the proposed electronic structure. Basic simplifications of the solid-state model used have been discussed. Examining the results of Compton scattering it is found that at small momenta the deviations of theory and experiment may be due to effects produced by the local-exchange-correlation approximation used. This should be particularly interesting since, using the IA, the Compton scattering of high-energy photons can be described very well by the ground-state properties of the valence electrons.[20]

ACKNOWLEDGMENTS

*Present address: Institut für Festkörperforschung, KFA Jülich, D-5170 Jülich, Germany.

[1] L. Hedin and S. Lundqvist, J. Phys. (Paris) 33, C3-73 (1972).

[2] O. Gunnarsson and B. I. Lundqvist, Phys. Rev. B 13, 4274 (1976).

[3] F. M. Mueller, A. J. Freeman, J. O. Dimmock and A. M. Furdyna, Phys. Rev. B 1, 4617 (1970).

[4] O. K. Andersen, Phys. Rev. B 2, 883 (1970).

[5] J. F. Janak, D. E. Eastman, and A. R. Williams, Solid State Commun. 8, 271 (1970).

[6] G. S. Painter, J. S. Faulkner, and G. M. Stocks, Phys. Rev. B 9, 2448 (1974).

[7] N. E. Christensen, Phys. Rev. B 14, 3446 (1976).

[8] V. L. Moruzzi, J. F. Janak, and A. R. Williams, in *Calculated Electronic Properties* (Pergamon, New York, 1978), p. 144; it should be noted that the lattice constant of our calculation (7.353 a.u.) is smaller than the one used by the mentioned authors (7.42 a.u.).

[9] L. F. Mattheiss, J. M. Wood, and A. C. Switendick, in *Methods of Computational Physics* (Academic, New York, 1968), Vol. 8, p. 63.

[10] P. Weinberger, K. Schwarz, and A. Neckel, J. Phys. Chem. Solid 32, 2063 (1971).

[11] Y. Onodera and M. Okazaki, J. Phys. Soc. Jpn. 21, 1273 (1966).

[12] S. Takada, Prog. Theor. Phys. 36, 224 (1966).

[13] P. Weinberger, R. Podloucky, C. P. Mallett, and A. Neckel, J. Phys. C 12, 801 (1979).

[14] A. Neckel, K. Schwarz, R. Eibler, P. Rastl, and P. Weinberger, Mikrochim. Acta Suppl. 6, 257 (1975).

[15] P. Weinberger, Theor. Chim. Acta 42, 169 (1976).

[16] P. Weinberger and F. Rosicky, Theor. Chim. Acta 48, 349 (1978).

[17] P. Weinberger, Theor. Chim. Acta 44, 315 (1977).

[18] W. Jones and N. H. March, in *Theoretical Solid State Physics* (Wiley, London, 1973), Vol. 1, p. 451.

[19] P. M. Platzman and N. Tzoar, Phys. Rev. 139, A410 (1965).

[20] P. Eisenberger and P. M. Platzman, Phys. Rev. A 2, 415 (1970).

[21] P. Eisenberger and W. A. Reed, Phys. Rev. B 9, 3237 (1974).

[22] S. Wakoh and J. Yamashita, J. Phys. Soc. Jpn. 35, 1402 (1973).

[23] F. Biggs, L. B. Mendelsohn, and J. B. Mann, At. Data Nucl. Data Tables 16, 201 (1975).

[24] P. Weinberger, Ber. Bunsenges. Phys. Chem. 81, 804 (1977).

[25] S. A. Nemnonov and M. F. Sorokina, Fiz. Met. Metalloved. 23, 732 (1967).

[26] K. Schwarz and A. Neckel, Ber. Bunsenges. Phys. Chem. 79, 1071 (1975).

[27] N. V. Smith, G. K. Wertheim, S. Hüfner, and M. M. Tramm, Phys. Rev. B 10, 3197 (1974).

[28] R. Harthoorn and P. B. Mijnarends, J. Phys. F 8, 1147 (1978).

[29] R. Lässer and B. E. Lengeler, Phys. Rev. B 18, 637 (1978).

[30] M. J. Martin and P. M. Blichert-Toft, Nucl. Data Tables A 8, 1 (1970).

[31] R. Lässer, B. Lengeler, and K. A. Gschneidner (unpublished).

[32] R. Harthoorn, Ph.D. thesis (Netherlands Energy Research Foundation, Petten, Netherlands, 1977), p. 88 (unpublished).

[33] P. Eisenberger and W. A. Reed, Phys. Rev. B9, 3242 (1974).